JOURNAL OF SPACECRAFT AND ROCKETS
Vol. 29, No. 6, November–December 1992

Hypersonic Single Expansion Ramp Nozzle Simulations

Stephen M. Ruffin*
NASA Ames Research Center, Moffett Field, California 94035
Ethiraj Venkatapathy* and Earl R. Keener*
Eloret Institute, Palo Alto, California 94303
and
Frank W. Spaid†
McDonnell Douglas Research Laboratories, St. Louis, Missouri 63166

The single-expansion ramp-nozzle experiment underway at NASA Ames Research Center simulates the National Aerospace Plane propulsive jet-plume flow. Recently, limited experimental data have become available from an experiment with a generic nozzle/afterbody model in a hypersonic wind tunnel. The present paper presents full three-dimensional solutions obtained with the implicit Navier-Stokes solver, FL3D, for the baseline model and a version of the model with side extensions. Analysis of the computed flow clearly shows the complex three-dimensional nature of the flow, critical flow features, and the effect of side extensions on the plume flow development. Schematics of the flowfield appropriate for the conditions tested are presented for the baseline model and the model with side extensions. The computed results show excellent agreement with experimental shadowgraph and with surface pressure measurements. The computed and experimental surface oil flows show the same features but may be improved by appropriate turbulence modeling.

Nomenclature

M	= Mach number
p	= pressure
Re/m	= Reynolds number per meter
T	= temperature
x	= streamwise coordinate
z	= vertical coordinate
α	= angle of attack

Subscripts

jet	= internal nozzle exit condition
t	= stagnation condition
∞	= freestream condition

Introduction to the Single-Expansion Ramp-Nozzle Experiment

HYPERSONIC air-breathing vehicles, such as the proposed National Aerospace Plane (NASP), require efficient airframe propulsion integration. A major element of the integrated design is the interaction between the jet-plume flow, the external flow, and the afterbody. The afterbody is designed as a single- (or one-sided) expansion ramp-nozzle (SERN) to minimize friction drag and nozzle weight while extracting thrust from the high-pressure flow on the afterbody. This complex interaction can significantly alter the thrust, pitching moment, and overall performance of the NASP.

Presented as Paper 92-0387 at the AIAA 30th Aerospace Sciences Meeting and Exhibit, Reno, NV, Jan. 6–9, 1992; received March 9, 1992; revision received July 16, 1992; accepted for publication July 17, 1992.

*Aerospace Scientist, Aerothermodynamics Branch, Thermosciences Division, MS 230-2. Member AIAA.

†Program Director, Experimental Fluid Dynamics, P.O. Box 516. Associate Fellow AIAA.

Existing ground-based test facilities can only simulate some aspects of the hypersonic flight environment. Therefore, accurate and validated computational fluid dynamics codes are needed to provide simulations of realistic flight conditions. The experimental validation data should, of course, model as many of the realistic flight conditions as possible. The validated codes can then be used to provide the most reliable predictions of the increments in performance or design parameters associated with the differences between the available test conditions and the flight environment.

An experiment has been conducted at NASA Ames Research Center that will allow greater insight into nozzle/afterbody flows relevant to the NASP. The SERN experiment was conducted in the NASA Ames 3.5 ft Hypersonic Wind Tunnel. This is a closed-circuit blow-down wind tunnel which has interchangeable, contoured, axisymmetric nozzles upstream of the test section. Figures 1 and 2 illustrate the primary features of the SERN model. The side view of the model is a parallelogram. The leading- and trailing-edge angles of the model are 20 deg. The upper surface of the model forward of the cowl is a flat plate with a sharp leading edge. A boundary-

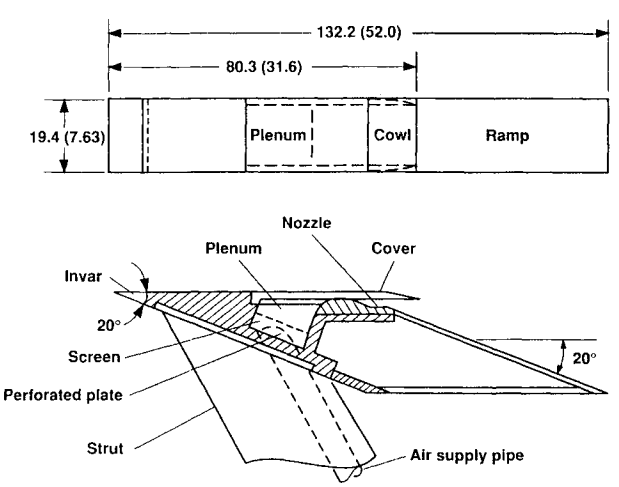

Fig. 1 Schematic of the baseline SERN model, [all dimensions are in cm (in.)].

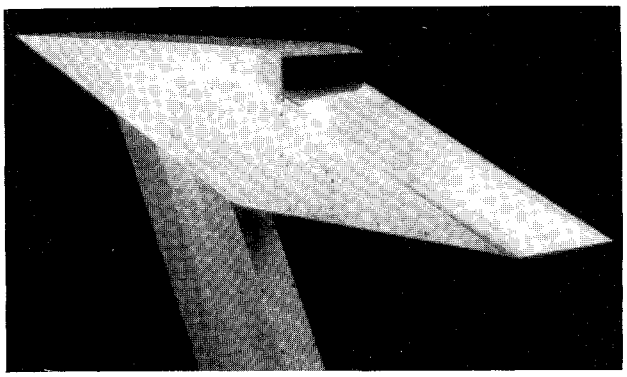

Fig. 2 Baseline SERN model.

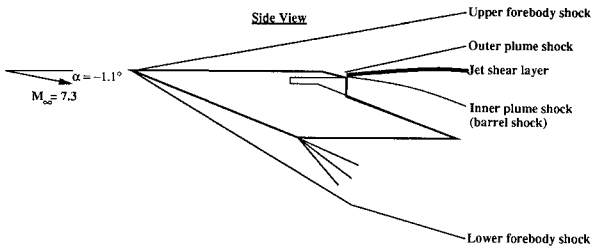

Fig. 3 Symmetry plane schematic of the SERN flowfield.

layer trip is located 10.2 cm (4 in.) downstream of the leading edge. This device causes rapid transition to turbulence on the forebody boundary layer and in the subsequent plume shear layer. A perforated plate is located at the entrance of the supply pipe to the plenum, followed by two screens. The internal nozzle downstream of the plenum was designed to provide uniform flow at the simulated combustor exit station. At the combustor exit station, the inviscid Mach number is approximately 1.5 and the expansion angle is 20 deg. A nozzle cowl 10.2 cm (4 in.) in length begins at the combustor exit station. The internal nozzle exit referred to in this study corresponds to the cowl exit station. Earlier versions of the model design included 15.2-cm- (6.0-in.) wide extensions that would attach to the side of the model and effectively increase the ramp width.

Table 1 gives the flow conditions used for the present computations. The entire model is immersed in a freestream flow of $M_\infty = 7.3$ and high pressure air exits the nozzle with a jet to freestream static pressure ratio of approximately 11. A number of parametric studies were performed during the experimental investigation to understand the flowfield development under different operating conditions.

Figure 3 shows the basic flow features in the symmetry plane of the SERN experimental model, and the details are described below. The flow is three-dimensional, but much of the flow development can best be explained with a side view. Crossflow views are given in a later section. The experimental model is oriented at a negative angle of attack with respect to the freestream. Leading-edge, or forebody, shocks are present both on the upper and lower surfaces of the model. The internal nozzle flow development is dictated by the contour of this nozzle, which is designed to be shock free. The internal nozzle shape is flat on the upper cowl and side walls and only the lower wall is contoured. Because of the one-sided contoured wall design, the flow at the exit of the nozzle will vary in the vertical direction but will be two-dimensional.

The interaction of the jet with the external flow is of main interest here. Similar to the plume flow associated with rocket nozzles,[1,2] the interaction between the expanding plume and the external flow produces an outer plume shock, a shear-layer, and an inner plume shock (i.e., barrel shock). Since the ramp surface limits the plume flow development, the outer plume shock, the shear-layer, and the inner plume shock will interact with the viscous wall layer on the ramp surface. The pressure differences between the upper and the lower surfaces of the model will induce a crossflow from the lower to the upper side and a complex vortical structure will exist. The interaction between the plume flow and this side edge flow will depend on the model geometry and flow conditions, such as angle of attack, etc. The static pressure ratio between the nozzle exit and the external flow primarily determines the size of the plume and the strength of the various flow structures associated with the plume. The pressure and skin friction on the external ramp surface determine the nozzle efficiency and the thrust. The pressure and skin friction values on the ramp surface are a result of the various interactions. In addition to the flow details just mentioned, the boundary layers and shear layers are expected to be turbulent. The flow may separate on the upper cowl surface due to adverse streamwise pressure gradient and there also may be a plume-induced crossflow separation which will be discussed in the results sections.[3] The major plume features will be present whether or not the flow separates on the cowl upper surface.

A variety of flowfield measurements have been taken both on the model surface and in the surrounding flow. At present, surface oil-flow patterns, shadowgraph visualization photographs, and surface centerline static pressures are available and are presented in this paper. Complete surveys of the plume flowfield and skin-friction data will be presented in a subsequent publication which also describes, in detail, the experimental program.

The experimental development has been supported by a computational effort. Earlier numerical studies were also used to help design this experiment. These efforts are described in greater detail by Ruffin et. al.[4] and by Venkatapathy et. al.[5] However, these preliminary computations were performed on an earlier model design with side extensions. In the present paper, three-dimensional Navier-Stokes solutions and two-dimensional symmetry plane solutions are presented for the baseline model at the nominal test conditions. Critical flow features are identified and the results are compared with experimental shadowgraphs, oil-flow visualization, and surface pressure data along the model centerline. For the three-dimensional cases, patched, and in some cases, solution-adapted grids are used to map the complex three-dimensional geometry. Simulations of a version of the model with 15.2 cm (6.0 in.) ramp side extensions are also presented. The effects of side extensions and other geometric features on SERN flow structure are discussed.

Solution Algorithm

The computations in this study are performed with FL3D, a three-dimensional, implicit time-marching Navier-Stokes solver. FL3D is a finite difference code that solves the Navier-Stokes equations in generalized coordinates. This code has previously been applied to axisymmetric and three-dimensional generic rocket nozzle plume flows.[1,2] All of the present calculations are for laminar flow of a perfect gas. The perfect-gas assumption is valid because both the freestream and jet static temperatures are sufficiently low. Much of the experimental flowfield will be turbulent because of the high Reynolds number and the

Table 1 Test conditions for computed solutions[a]

	Condition 1	Condition 2
M_∞	7.3	7.4
α, deg	0.0	−1.1
T_∞, K	57.2	71.5
p_∞, Pa	756	673
Re/m	1.2×10^8 m^{-1}	1.5×10^8 m^{-1}
p_{tjet}/p_∞	300	337
T_{tjet}/T_∞	5.0	3.9
p_{jet}/p_∞	10.6	≈ 10.7
M_{jet}	2.83	≈ 2.87

[a]Both the freestream and jet gas are air.

boundary-layer trip on the upper model surface. The present laminar flow calculations are designed to give an understanding of the overall flow structure and primary flow features. When more detailed, calibrated experimental data become available, quantitative comparisons with turbulent flow predictions will be conducted.

This numerical formulation is detailed by Obayashi[6] and only briefly outlined here. The numerical method is a lower-diagonal-upper (LDU), alternating-direction-implicit (ADI) scheme with Roe's averaging. The LDU-ADI algorithm is a diagonal algorithm requiring minimal CPU per iteration and is applicable to steady flows. High-order spatial accuracy is achieved by constructing monotone upstream-centered scheme for conservation laws (MUSCL) differencing with a differentiable limiter. The ADI sweeps of this formulation are quite efficient. Venkatapathy and Feiereisen[2] used this method to predict plume flows accurately. This scheme has been applied to complex plume flows and the solutions were validated in terms of shock reflection location and plume structure for highly underexpanded axisymmetric plume flows. The calculations were performed both with supersonic external flow and with quiescent ambient conditions.[4] The success of the solver in these limited validations permits confidence in the present solutions for the experimental SERN flowfield.

Grid Generation

The computational grids used in this study are created with an algebraic grid generation code. This code utilizes bilinear interpolation to provide smoothly varying grid planes with nearly orthogonal grid cells. To map the complex SERN geometry, multiple grid zones are generated. The surface grid and the boundaries of each grid zone are shown in Fig. 4 for the baseline model. This grid consists of 13 grid zones. Although not shown in Fig. 4, each of the grid zones overlaps its neighbor by one common grid plane. The flow solver alternates grid zones on which it computes and applies the appropriate boundary condition on each of the intersecting grid planes. The computed results show seamless contours of all flow variables. The three-dimensional flow computation on the baseline model was performed with 338,000 total grid points and required approximately 5 h of CPU time on a Cray YMP computer.

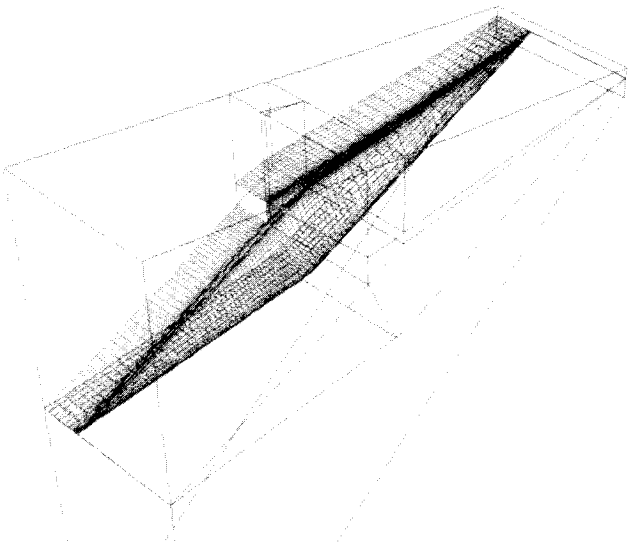

Fig. 4 Surface grid and grid zone boundaries for baseline model computations.

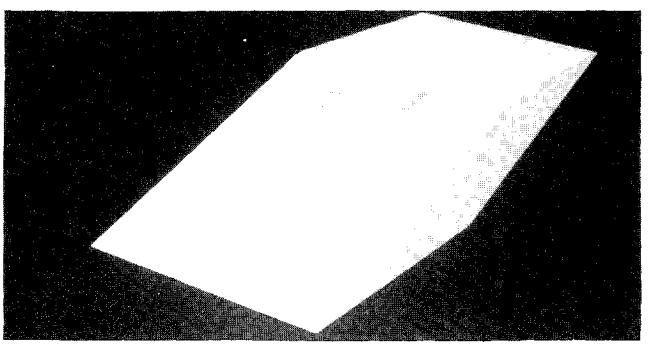

Fig. 5 Computational body for model with 15.2-cm- (6.0 in.) wide side extensions.

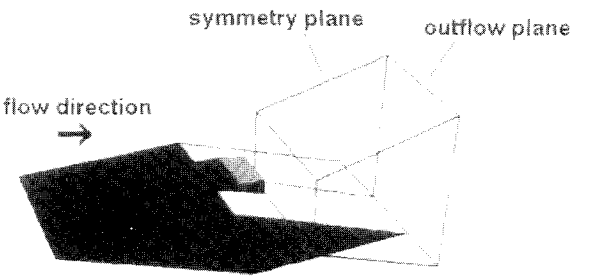

Fig. 6 Plume region for computations on the model with side extensions.

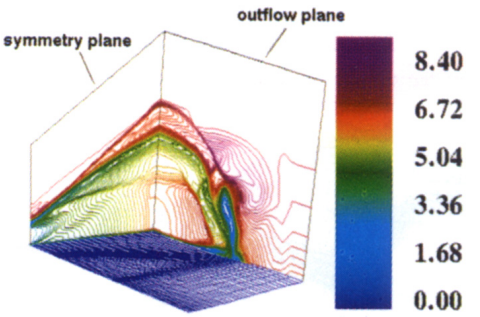

Fig. 7 Computed Mach contours in the symmetry and outflow planes in the plume region of the model with side extensions.

Boundary Conditions

The boundary conditions encountered in the present nozzle/afterbody calculations are inflow or outflow, wall boundaries, symmetry, and reflection boundaries. All of the boundary conditions were applied explicitly. At the supersonic inflow boundary, conservative flow variables were frozen, and at the outflow, flow variables were extrapolated from the interior. At the wall boundary viscous, no-slip, adiabatic wall boundary conditions were applied. In the case of symmetry boundaries, the flow variables were simply reflected from the interior. The various boundary conditions were unified into one generalized routine so that any specified part of the computational domain could be updated with the proper boundary condition. This unified boundary-condition formulation greatly facilitated the use of three-dimensional zonal grids needed to map the experimental geometry.

Three-Dimensional Results on the Model with Side Extensions

One of the afterbody design considerations for hypersonic vehicles is the width of the afterbody surface. This geometric factor influences total vehicle thrust due to nozzle plume pressure and skin-friction drag on the afterbody. To study the effects of ramp width, calculations of a version of the model with 15.2 cm (6.0 in.) side extensions were conducted. These calculations were performed at condition 1 shown in Table 1. For this case, the internal nozzle flow was not computed. Instead, the jet flow at the nozzle exit is modeled by specifying inviscid conditions and approximate boundary-layer profiles. The boundary-layer profiles are specified by using the Pohlhausen polynomial approximation[7] for the velocities and the Crocco-Busemann relation[8] for compressible boundary layers for the temperature profile. Figure 5 shows the compu-

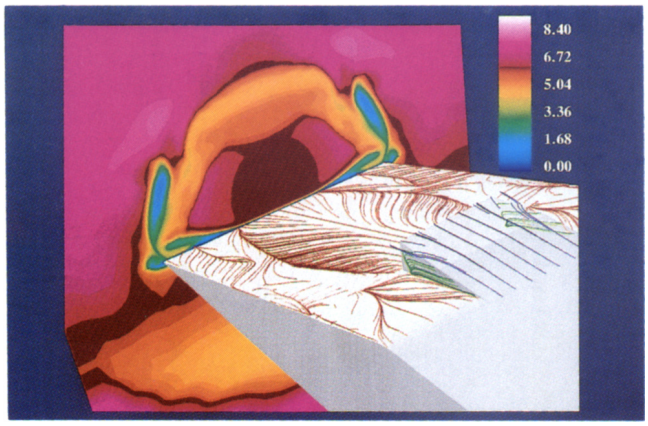

Fig. 8 Simulated surface oil-flow pattern and Mach contours in the outflow plane for model with side extensions.

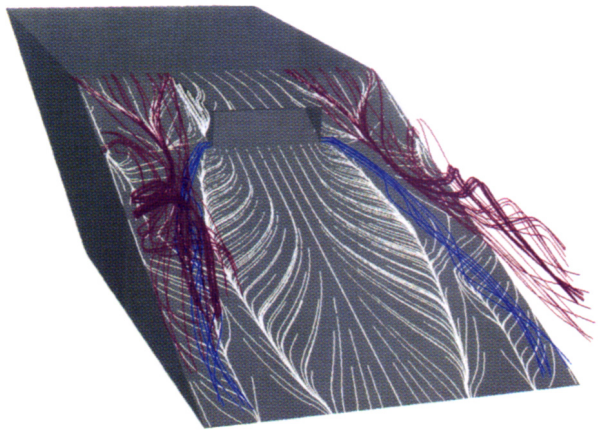

Fig. 9 Simulated surface oil-flow pattern and particle traces for the model with side extensions.

tational model for this case. For this simulation a solution-adapted grid was used. The three-dimensional adapted grid package used clusters existing grid points in regions of high flow gradients and is described by Davies and Venkatapathy.[9] For the present case, the grid was adapted on gradients of both Mach number and static temperature. Figure 6 outlines the plume region and shows the location of the symmetry and outflow planes. Figure 7 gives computed Mach contours in these two planes. The solution was adapted on gradients of both temperature and Mach number so that good resolution of the plume shocks and shear layers is achieved.

The symmetry plane Mach contours in Fig. 7 predict the outer plume shock, shear layer, and inner plume shock (i.e., barrel shock) shown in the schematic in Fig. 3. This calculation is performed for the model at zero angle of attack. In the outflow plane at the end of the ramp, the Mach contours also show these features and indicate that the width of the plume extends laterally to near the side edge of the model. The Mach contours in this outflow plane also indicate a complex viscous structure near the intersection of these plume shocks with the ramp and another complex structure just outside the plume boundary. These features can be further understood by studying Figs. 8 and 9. Figure 8 shows simulated oil flow and the Mach contours in the outflow plane, and Fig. 9 shows particle traces and simulated surface oil-flow pattern. For the model with side extensions, the freestream flow expands in the region above the side extension ramp surface. The magenta particle traces in Fig. 9 correspond to a large vortex that is generated in this expanding region above the side extensions. As the flow proceeds downstream, this side extension vortex lifts off the ramp surface and follows the outside edge of the outer plume shock. The blue particle traces correspond to a vortex that begins from the trailing-edge corner of the cowl and follows the outer boundary of the plume along the surface of the ramp. The most prominent features in the predicted oil-flow pattern are crossflow separation lines which extend from the cowl to the ramp trailing edge. These separation lines are clearly within the plume external shock boundary and approach the symmetry line of the model as they proceed downstream. These features correspond to crossflow separation induced by the inner plume shock (barrel shock) within the plume. The expanding crossflow from the symmetry line experiences a strongly adverse pressure gradient from the internal plume shock and crossflow separation is induced.

Based on the results presented, a schematic of the cross-sectional SERN flow is developed and is shown in Fig. 10. This flow schematic is appropriate in the plume region of the flow at the conditions given in Table 1. The large side extension vortex lifts off the ramp surface and interacts with the outer plume shock. Near the ramp, the inner plume shock induces a primary crossflow separation vortex whose separation line is very prominent in the surface oil-flow pattern. Underneath this vortex, a secondary crossflow vortex is found to exist.

Results on the Baseline Model

Computations on the baseline SERN model without side extensions were conducted at condition 2 shown in Table 1. For this simulation the internal nozzle flow was computed and solved coupled to the other grid regions. Predicted Mach contours in the symmetry and outflow planes for the baseline experimental model are shown in Fig. 11. The symmetry plane shows the same features in the plume region as preceding computations on the model with side extensions. The calculations on the baseline model and the experiment were performed with the model at a -1.1 deg angle relative to the freestream and the forebody produces a shock on the upper side of the model. From the outflow plane, we see that the

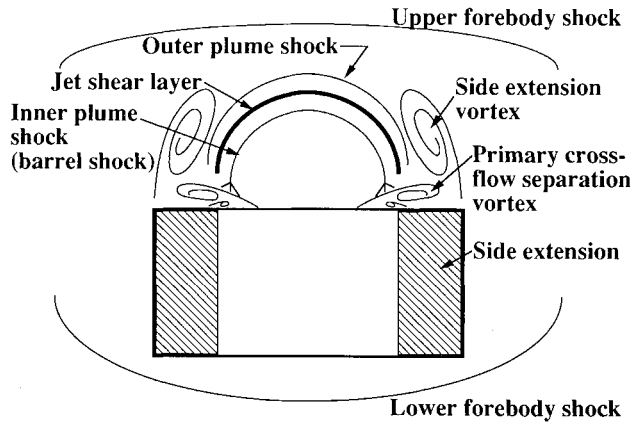

Fig. 10 Cross-sectional schematic of the plume flowfield for the model with side extensions.

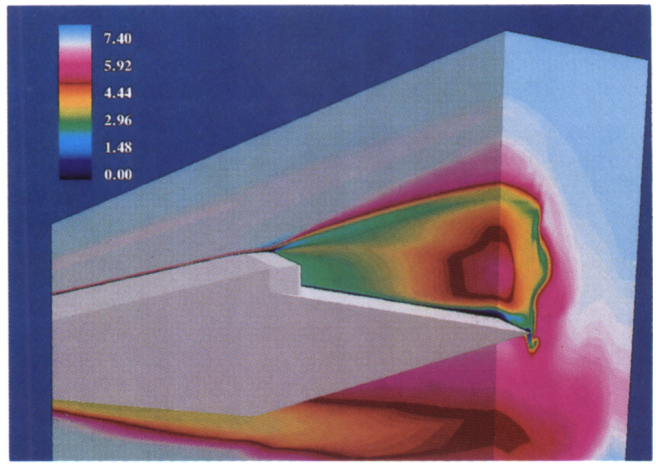

Fig. 11 Computed Mach contours in the symmetry and outflow planes for the baseline model.

width of the plume extends to the side edge of the body. Particle traces and velocity vectors which are not shown indicate a number of vortices near the model side edge. The overall plume flow structure in the crossflow plane for the baseline model is shown in Fig. 12 for these flow conditions. The outer plume shock extends laterally over the side edge of the model and approaches the side corner of the model near the ramp. This shock induces a vortex on the side of the model. As in the model with side extensions, the inner plume shock induces a primary crossflow separation vortex, which is accompanied by a smaller secondary vortex. Because the baseline model has no side extensions, the large side extension vortex present in the preceding results does not exist for the baseline model.

Surface pressure measurements have been taken at a variety of locations on the model ramp. At present only data along the centerline is available. Figure 13 shows a comparison of the experimental and computed static pressure along the ramp centerline. The computed results show excellent agreement with the experimental data.

The symmetry plane flow is of interest for two reasons. First, although experimental surveys of several crossflow planes will be available, the most detailed data will be obtained along the symmetry plane. Also, very fine grids can be used in two-dimensional simulations to resolve critical flow features without prohibitive CPU requirements. For these two reasons, it is of interest to know if the three-dimensional features affect the symmetry plane flow. To study three-dimensional effects on the symmetry plane flow, two-dimensional symmetry plane results were compared to the predicted symmetry plane flow from a three-dimensional calculation. The symmetry plane grid contains 80×60 grid points. Figure 14 shows Mach-number surveys at three streamwise locations for the three-dimensional and two-dimensional cases on the same grid. The $x = 63.0$ cm (24.8 in.) station is upstream of the nozzle cowl. The $x = 106.4$ cm (41.9 in.) station is in the plume region midway between the internal nozzle exit and the end of the ramp, and the $x = 129.8$ cm (51.1 in) station is in the plume region at the end of the afterbody ramp. It is found

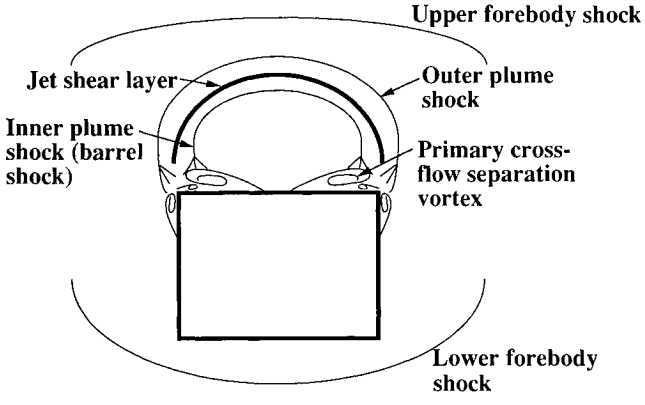

Fig. 12 Cross-sectional schematic of the plume flowfield for the baseline model.

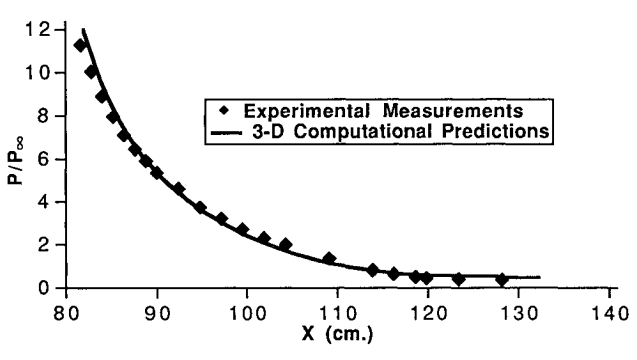

Fig. 13 Comparison of computed and experimental surface static pressure along the baseline model centerline.

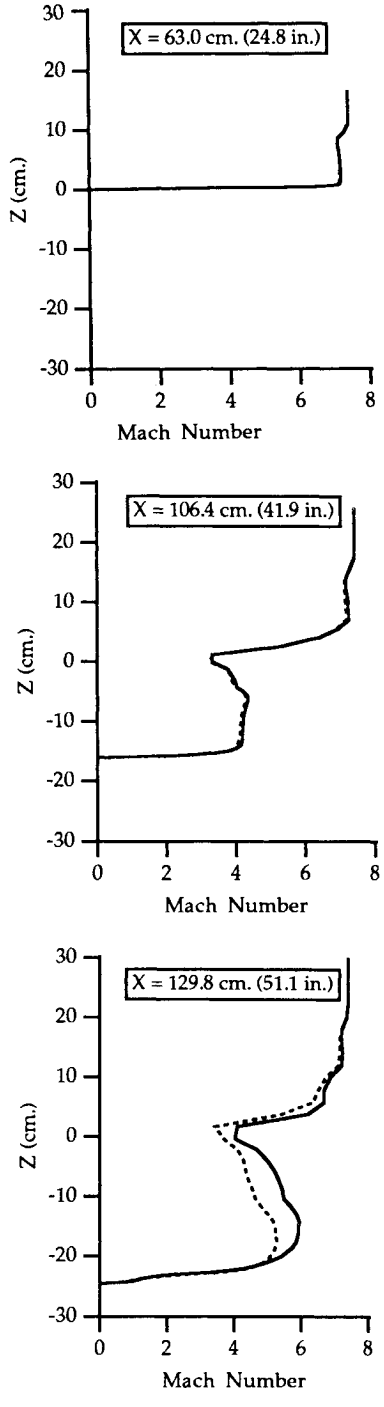

Fig. 14 Comparison of symmetry plane Mach number at three streamwise stations for three-dimensional and two-dimensional calculations. Solid line: three-dimensional solution; and dashed line: two-dimensional solution on the same symmetry plane grid.

that the three-dimensional features do not significantly affect the symmetry plane flow until near the trailing edge of the model. Similar comparisons of two-dimensional and three-dimensional results in the symmetry plane[4] also revealed little difference between the two simulations. However, overall the flow does expand somewhat faster in the three-dimensional case due to pressure relief in the crossflow direction.

Calibration data obtained with the Mach 7.3 wind-tunnel nozzle used during the experimental investigation show the presence of a moderate degree of expansion (source flow) in the test section. For most of the computational simulations this gradient was neglected, and uniform external-flow conditions were imposed on the inflow boundaries of the computational domain. To evaluate the effect of the nonuniform exter-

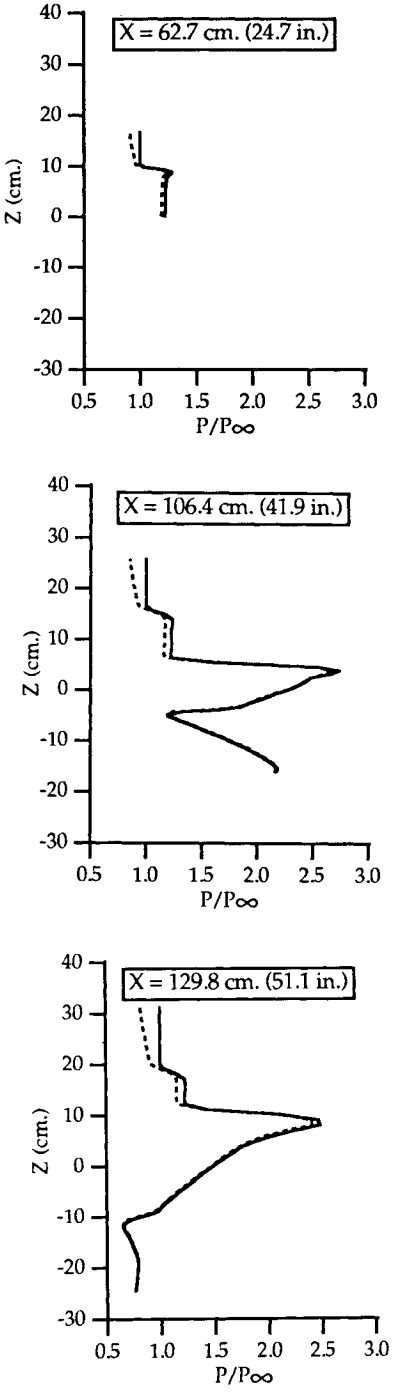

Fig. 15 Comparison of symmetry plane pressure at three streamwise stations for flow with uniform freestream and flow with expanding freestream variation. Solid line: uniform freestream; and dashed line: expanding freestream.

nal flow and to study any interaction between the nonuniform freestream and the jet plume, numerical experiments were conducted with uniform and expanding freestream flow conditions. These numerical experiments were limited to two-dimensional symmetry plane computations with a 159×119 grid. In the tunnel test section, a normalized pressure change of $\Delta p/p_\infty = -0.138$ and Mach number change of $\Delta M_\infty = 0.178$ were measured. In the two-dimensional simulations these gradients were imposed, and through isentropic relationships[10] the freestream conditions and the conservative flow quantities at all of the inflow and top boundary grid points were computed. In the uniform freestream case, the flow conditions corresponding to condition 2 in Table 1 was maintained at all grid points on the top and inflow boundary surfaces. Both cases were computed with the same nozzle sonic throat conditions for the internal nozzle. Static pressure profiles, along the z direction, at three streamwise locations, are compared in Figs. 15a–15c. Pressure contours from the computed solutions with uniform and nonuniform freestream conditions are shown in Fig. 16a and 16b, respectively. The computed solutions show that the nonuniform freestream conditions affect only the flow above the jet-plume region. The upper forebody shock shape and the conditions behind the shock are affected by the conditions upstream of this shock, but the shock acts as a buffer to reduce the effect of the nonuniformities in the freestream. The outer plume shock has a similar damping effect, and the flowfield in the vicinity of the jet closely resembles that of the uniform flow case. The ramp surface pressure and the flow inside the plume are unaffected by the nonuniform external flow. Although the numerical experiments were carried out only along the symmetry plane, as a two-dimensional study, these conclusions are also expected to hold in the three-dimensional case.

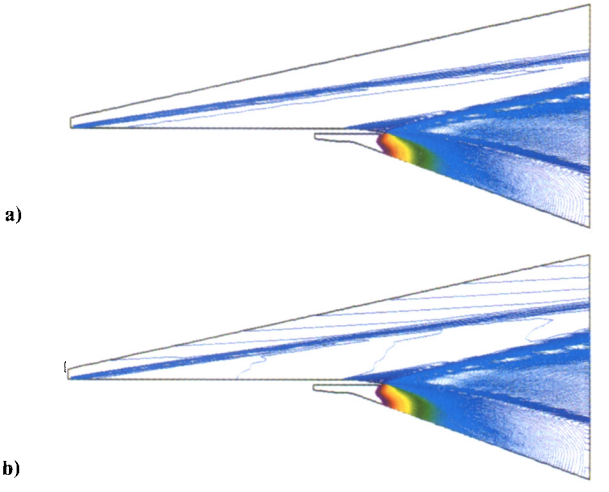

Fig. 16 Comparison of symmetry plane pressure contours: a) uniform freestream; and b) expanding freestream.

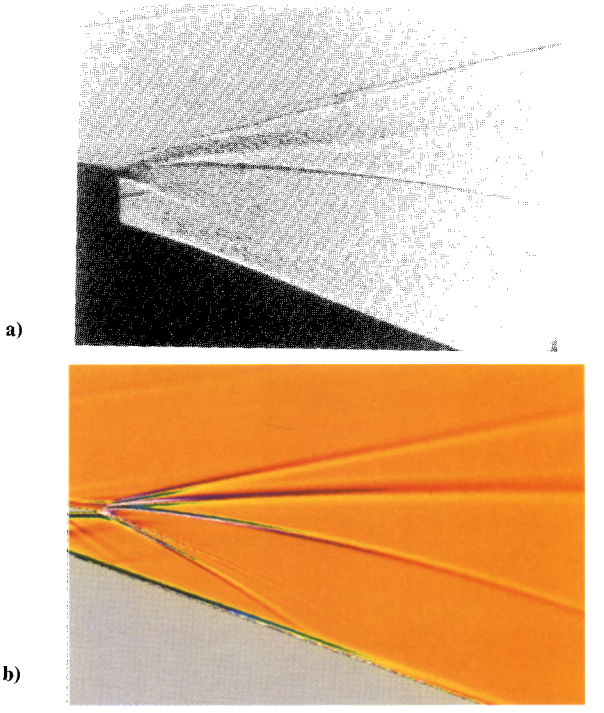

Fig. 17 Experimental and computational shadowgraphs in the symmetry plane of the baseline model. Simulated shadowgraph is based on two-dimensional fine grid results: a) experimental; and b) computational.

An experimental shadowgraph photograph and a simulated shadowgraph based on a fine grid symmetry plane calculation are shown in Fig. 17. The fine grid consisted of 300 × 300 grid points. The forebody shock, outer plume shock, shear layer, and barrel shock are resolved quite well. The location of these features agrees well with the computed results. The downward curve of the upper cowl surface induces a streamwise boundary-layer separation near the trailing edge of the cowl. The curved outer boundary of the cowl followed by the shear layer between the underexpanded jet and the freestream produces an effective compression corner. One difference between the experimental and computed results is that the experimental boundary layers and shear layers are turbulent. The experimental shadowgraph shows a thick turbulent boundary layer on the model forebody which feeds into a thick plume shear layer. The laminar flow calculations of course do not reproduce these turbulent details but predict the overall symmetry plane flow quite well.

The experimental surface oil-flow patterns on the afterbody ramp is shown in Fig. 18a. Predicted surface oil-flow patterns for the baseline model and the model with side extensions are shown in Figs. 18b and 18c. In the experimental oil pattern, the flow appears to be two-dimensional inside the cowl, with no separation at the corner. The pattern on the ramp is symmetrical and the centerline flow is straight down the ramp. The surface flow direction turns increasingly outboard with increasing distance from the centerline. The prominent crossflow separation lines on the ramp predicted in both of the computed results are also observed experimentally. As is evident from the oil-flow patterns and indicated in schematics in Figs. 10 and 12, the primary crossflow separation lines are found to exist closer to the symmetry line for the baseline model relative to the model with side extensions. The rate at which these separation lines approach the symmetry line toward the trailing edge is different in the predicted vs the experimental results. The details of this viscous dominated effect may be strongly influenced by turbulence which is not modeled. In all of the oil-flow patterns, a secondary crossflow separation line is also seen near the side edge of the model. In addition, the experimental oil-flow pattern shows a streamwise separation line on the upper surface of the cowl near the trailing edge. This separation is also apparent from the computational and experimental shadowgraphs in Fig. 17.

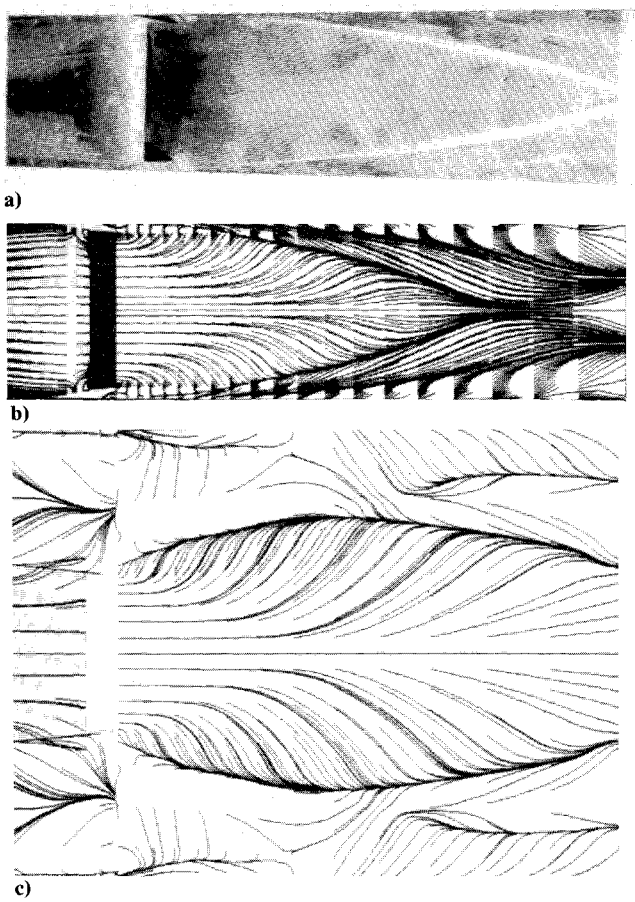

Fig. 18 Experimental and simulated oil-flow on the ramp surface: a) experimental on baseline model; b) simulated on baseline model; and c) simulated on model with side extensions.

Concluding Remarks

The latest version of FL3D, an implicit, three-dimensional Navier-Stokes solver, is used to predict the experimental hypersonic flowfield. Multiple, and in some cases, solution-adapted grids are used to map the three-dimensional nozzle/afterbody geometry. Roe's averaging and MUSCL differencing are used to model critical flow features. These modifications have greatly improved the efficiency of the code and its ability to provide accurate modeling of complex flowfields. Three-dimensional calculations of the two SERN geometries and two-dimensional symmetry plane calculations have been performed which simulate the cold-jet perfect-gas experimental conditions. Flow schematics appropriate for the conditions tested are presented for the baseline model and the model with side extensions.

The computed results show excellent agreement with experimental shadowgraph and with centerline surface pressure measurements. The computed and experimental surface oil flows show favorable agreement but demonstrate the need for turbulence modeling. At present, several candidate algebraic and two-equation turbulence models are being validated in jet plume flows. Turbulent code-validation cases will be conducted and presented along with detailed calibrated experimental data in a subsequent publication. All of the flow features observed experimentally are also seen in the computed results, thus the success of the current predictions with the available data is quite promising.

Acknowledgments

Support for E. Venkatapathy was provided by NASA Grant NCC2-420. Support for E. Keener was provided by NASA Grant NCC2-553.

References

[1]Venkatapathy, E., and Feiereisen, W. J., "3-D Plume Flow Calculations with an Upwind Solver," AIAA Paper 88-3158, July 1988.

[2]Venkatapathy, E., Feiereisen, W. J., and Obayashi, S., "Computational Studies of Hard Body and 3-D Effects in Plume Flows," AIAA Paper 89-0129, Jan. 1989.

[3]Venkatapathy, E., and Feiereisen, W. J., "Computational Analysis of Plume Induced Separation," AIAA Paper 91-0711, Jan. 1991.

[4]Ruffin, S. M., Venkatapathy, E., Keener, E. R., and Nagaraj, N., "Computational Design Aspects of a NASP Nozzle/Afterbody Experiment," AIAA Paper 89-0446, Jan. 1989.

[5]Venkatapathy, E., Ruffin, S. M., Lee, S. H., Deiwert, G. S., and Feiereisen, W. J., "Development and Applications of a Nozzle/Afterbody Flow Solver," NASP CR-1068, Jan. 1990.

[6]Obayashi, S., "Numerical Simulation of Underexpanded Plumes using Upwind Algorithms," *Proceedings of the AIAA Atmospheric Flight Mechanics Conf.* (Minneapolis, MN), AIAA, Washington, DC, Aug. 1988, pp. 284–299; see also AIAA Paper 88-4360, Aug. 1988.

[7]Pohlhausen, K., "Zur näherungsweisen Integration der Differentialgleichung der Grenzschicht," *Zeitschrift fuer Angewandte Mathematik und Mechanik*, Vol. 1, 1921, pp. 252–268.

[8]White, F. M., *Viscous Fluid Flow*, McGraw-Hill, New York, 1974, p. 587.

[9]Davies, C. B., and Venkatapathy, E., "Application of a Solution Adaptive Grid Scheme, SAGE, to Complex Three-Dimensional Flows," AIAA Paper 91-1594, June 1991.

[10]Anon., "Equations, Tables, and Charts for Compressible Flow," NACA Rept. 1135, 1953.

Michael E. Tauber
Associate Editor